RE . . . 27:11–24 (1989)

966

Modeling Surface Temperature Distributions in Forest Landscapes

H. R. Holbo
J. C. Luvall
Science and Technology Laboratory,
NASA Stennis Space Center

Frequency distributions of the spatial variability in surface temperature are examined and modeled. Surface temperature data were obtained from thermal images, acquired using NASA's Thermal Infrared Multispectral Scanner (TIMS). Two daytime and two nighttime overflights, from different forest management units on the H. J. Andrews Experimental Forest in the Cascade mountains of western Oregon, were made during August 1985. Prior to analysis, TIMS temperature values were corrected for atmospheric attenuation and emission of thermal radiation using the LOWTRAN-6 algorithm. Surface temperatures ranged from 10 and 60°C. Frequency distributions of these spatial temperature fields exhibited patterns that are closely associated with the nature of the surface coverage on the unit. The frequency distribution patterns of surface temperature were modeled using a two-parameter beta probability density distribution. The fit of the model was evaluated against the TIMS dataset. The parameters represent a mathematical description of the thermal signature of the distribution. The model's parameters provide a basis for identifying and classifying surface types. Model discrimination among the various surfaces was good for thermal images taken during the day. The model yielded a comparable, but less distinct, nighttime ranking.

Address correspondence to Dr. J. C. Luvall, Science and Technology Laboratory, HA10, Stennis Space Center, MS 39529.
Received 4 February 1988; revised 28 October 1988.

INTRODUCTION

Thermal infrared measures of plant and soil surface temperatures have been used since the 1960s (Gates, 1962) to investigate how these surfaces react to and/or influence, environmental energy flows. Most of this research has concentrated on uniform and homogeneous agricultural surfaces, focusing primarily upon soil moisture, plant water status, crop yield, and evapotranspiration relationships. Some examples are Bartholic et al. (1972), Soer (1980), Price (1980; 1982), Idso et al. (1975; 1977), Seguin and Itier (1983), Stone and Horton (1974), Hatfield et al. (1983; 1984), Heilman et al. (1976), Seguin (1984), and Reginato et al. (1985). These studies employed a wide variety of thermal radiance sensors, ranging from hand-held and ground-operated instruments to aircraft-mounted and satellite-based systems, and exhibiting resolutions from leaf-sized to hundreds of meters.

These same thermal response issues are of concern to investigators of natural landscapes (Balick and Wilson, 1980; Fritschen et al., 1982).

However, the analytical complexity and sampling tasks introduced by the surface heterogeneity that is characteristic of forests and other complicated landscapes has limited research about their environmental response relationships to the individual components of the system (e.g., Vanderwaal and Holbo, 1984). In fact, even though a substantial amount of thermal variability for these kinds of surface can be anticipated (Holbo and Childs, 1987; Holbo et al., 1985; Childs et al., 1985), quantitative measures of the spatial character of surface temperature heterogeneity at scales which can be identified on the ground have largely been lacking. This would require a remote-sensing means of thermally scanning entire surface types and mixtures of types (plants and soils), simultaneously, as they express their temperature responses to the same atmospheric and radiant inputs.

The inclusion of surface thermal process information in global-scale climate models is clearly recognized (Shukla and Mintz, 1982). But far more detailed information about the thermal response characteristics of heterogeneous surface types is needed (Carson, 1982; Dickinson, 1983; Carlson, 1986).

This report addresses the information needs in both of these areas. It describes the spatial attributes of surface temperature images obtained from a forested, mountainous landscape. Our specific objective in this initial investigation is to characterize and classify, using a data-modeling approach, several of the types of surface temperature frequency distributions that occur in that landscape.

SURFACE TEMPERATURE OBSERVATIONS

Observational Capabilities

Quantitative measures of surface temperatures at suitable spatial scales can be accurately obtained using the calibrated Thermal Infrared Multispectral Scanner (TIMS) (Palluconi and Meeks, 1985). This aircraft-mounted instrument acquires raster-scanned thermal radiance images in each of six spectral channels between 8 and 12 μm. In-flight referencing to calibrated blackbodies at the end of each raster assure the temperature accuracy of the data. The noise equivalent temperature specification for TIMS data is 0.09°C. This instrument's optical design, together with its sampling rate, affords a ground resolution of 5–30 m, depending upon flightline altitude. This spatial resolution is on the order of many surface features. Because it is aircraft-mounted, surfaces can be reimaged at short time intervals. The TIMS is thus an excellent tool for investigating surface temperature heterogeneity at the landscape scale.

Corrections to TIMS measurements are required because errors are introduced as thermal radiation passes through the atmosphere. Along this pathway both attenuation and emission of thermal radiation occurs that tend to diminish scene contrast and to shift radiance values. In clean and cloud-free atmospheres, compensation for these errors can be accomplished when air temperatures and humidities along the path between the surface and the aircraft are known.

Study Area

The area selected for thermal imaging is the H. J. Andrews Experimental Forest. It is a 6500 ha watershed located in the central-western Cascade Mountains of Oregon, with elevational extent from 400 to about 1500 m, east of Eugene, OR. The Andrews is one of the National Science Foundation's Long Term Ecological Research (LTER) sites. It represents the dense coniferous forests of Douglas-fir, western hemlock, and common true firs of the western slope of the Cascades (Hawk et al., 1978). Geological parent materials range from older andesites to younger basalts, much of which has been heavily altered or metamorphosed. Prior to its selection as a LTER, the watershed had been a USDA-Forest Service Experimental Forest. It provides a variety of forest stand ages and site exposures, and includes many diverse examples of forest management practices, including clearcut logged areas, partially logged or thinned or shelterwood areas, naturally regenerating areas, and monoculture plantations.

TIMS Data Collection

A series of four TIMS overflights covering the Andrews Experimental Forest were conducted on 5 August 1985. The flight paths provided image overlap from altitudes yielding an average ground resolution (pixel size) of 10 m at nadir. The daytime overflights were close to solar noon, to ac-

quire thermal images when solar irradiance was changing the least. The first began at 13:37 local time (PDT), the second 28 min later (14:06). Night flights began shortly after sundown, when radiant cooling rates would be high, the first at 21:41, the second 12 min later (21:53). Coincident sets of near-infrared color photographs were also taken as an aid in extracting ground-feature-referenced sites from the more abstract TIMS data files. No clouds were evident during any of these periods. The surface temperatures reported in this study are based on radiance measurements from TIMS's Channel 2 (8.4–9.2 μm).

Atmospheric Correction and Surface Temperature

Atmospheric profiles of air temperature and humidity were measured with radiosondes just prior to the noon and early evening flight times. The launch site was at 436 m, balloon ascent rate was initially 6 m/s, and data was telemetered at 3-s intervals through altitudes well above mission flight levels. This information enabled TIMS data to be subsequently corrected for errors due to thermal radiance attenuation and thermal emission along the atmospheric path between the surface and TIMS. The profile measurements were input to the LOWTRAN-6 model (Kneizys et al., 1983). The output from LOWTRAN-6 was later combined with TIMS spectral response calibration curves and in-flight blackbody reference measurements to produce the transform table for converting pixel data values to surface temperatures (Graham et al., 1986; Anderson, 1985).

Site Selection

From within the thermal image data files of the Andrews, we selected 10 sites for analysis. To minimize a real distortion, the sites chosen were within 10° of flightline nadir. In addition to five forest stands, we chose a clearcut unit, a shelterwood, a naturally regenerating unit, a plantation, and a rock quarry.

All sites were assigned four-letter identification codes for file handling and LTER reference purposes. The five forested sites are: AS32, RS07, RS10, RS18, and a stand of mature forest adjacent to RS18 we designated as OLDG. The clearcut unit is Snowbrush, or SNOW; the shelterwood is Mendel-2, or MNDL; the naturally regenerating stand is L341; the Douglas-fir plantation is L521; and the quarry we called simply ROCK.

Each of these sites was isolated from the larger flight line data files by individually delineating and extracting them as separate datasets (Sader, 1986). The delineation procedure was subjective, and involved manually tracing the borders of each site as the thermal image was displayed on a monitor, thereby entering into the computer the necessary coordinates for extracting the desired dataset. Contrast levels at the borders of the sites were not always adequate on the thermal image to afford complete confidence in its position, so the lines were usually traced slightly to the interior of the site. Generally, this still afforded a pixel population of 1000, or more, each nominally 0.01 ha in size. Our main concern during this operation was to acquire datasets uncontaminated by bordering areas that may have different surface characteristics, and to assure that the characteristics of the selected sites matched either LTER records or our on-the-ground site checks.

Surface Temperature Patterns

Figure 1 illustrates the frequency distribution patterns observed for six of the 10 sites at the H. J. Andrews Experimental Forest. Data for all flights is in one graph for each site.

Fig. 1a) shows the type of frequency distribution pattern typically observed from the fully developed Douglas-fir forest canopies, which comprised five of the thermally-imaged sites in this study. This example is OLDG. The frequency distributions for both the day and night from these forest-covered surfaces are narrow and symmetrical, the nighttime ones especially so. In the figure, the second day-data frequency distribution (D2) can be seen shifted toward higher temperatures, with a sharper peak than the first day-data frequency distribution (D1). Although difficult to discern from the figure, the night-data exhibit an opposite trend, shifting toward cooler temperatures.

Many of the same features are evident in Fig. 1b), which is from the Douglas-fir plantation (L521). The distributions for the plantation are broader and lower than the forest, and are less symmetrical, with frequency values which trend gradually toward higher temperatures in the day, and toward cooler at night. The open, less dense

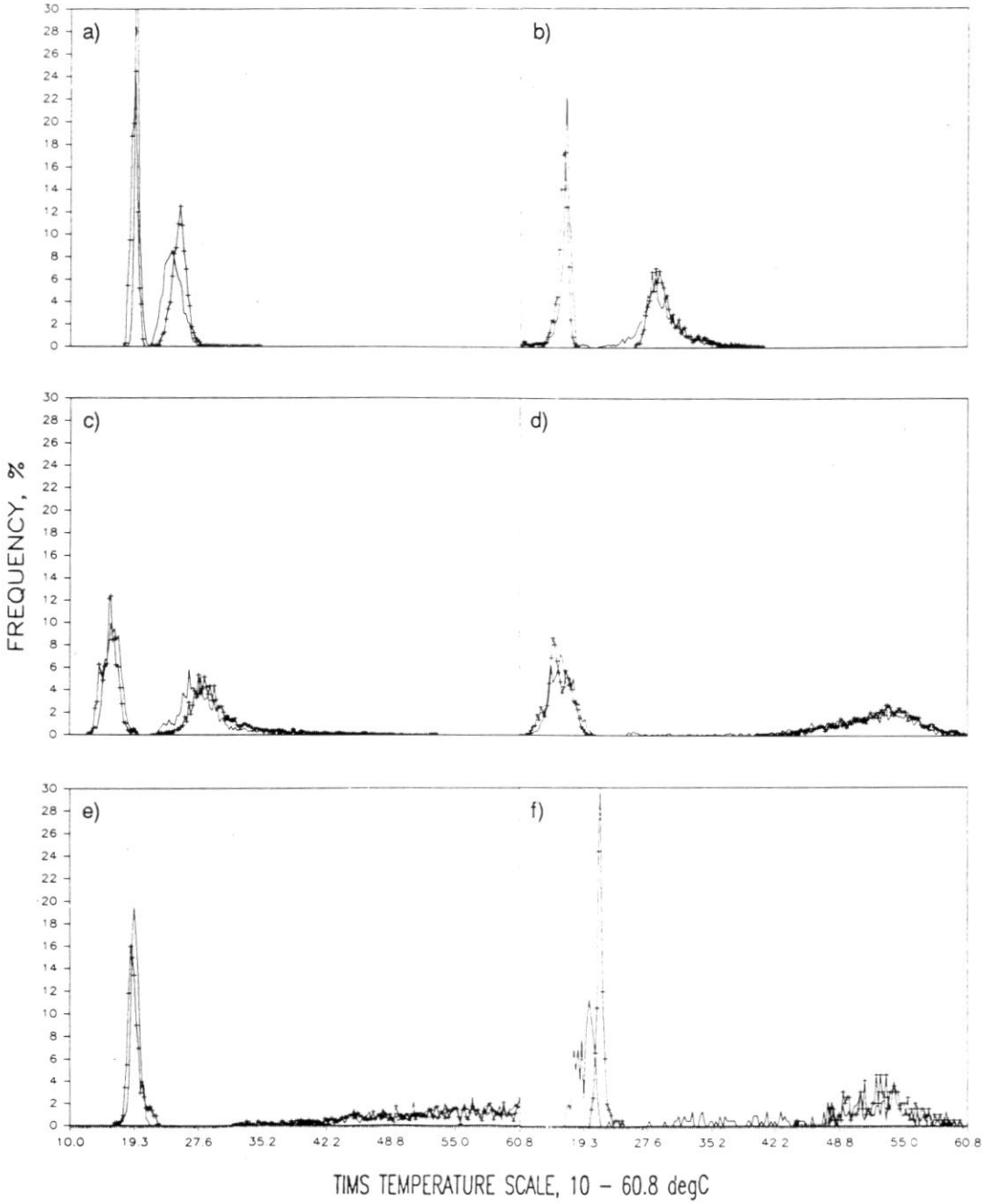

Figure 1. Frequency distributions of surface temperature at six of the 10 sites at the H. J. Andrews Experimental Forest (approx. 44°N latitude) on 5 August 1985: a) mature Douglas-fir forest (OLDG); b) Douglas-fir plantation (L521); c) natural regeneration, with Douglas-fir and maple (L341); d) a recently clearcut-logged site (SNOW); e) shelterwood site (MNDL); f) a rock outcrop and quarry (ROCK). Each subfigure shows the observations for each site from both daytime and both nighttime overflights. The higher temperature 1st day data (D1) and lower temperature 1st night data are lines only. The 2nd day data (D2) and 2nd night data (N2) lines are denoted with symbols. Except for the quarry [f)], which was a small site with an image size of only 100 pixels, all frequency distributions shown are based on image datasets containing 1000 or more 0.01 ha pixels.

canopy of these sites allowed the underlaying soil and forest floor materials to influence the radiance distribution.

At the natural regeneration site (L341), Fig. 1c), the patterns become more diffuse in character. The frequency distributions from both daytime datasets are broader, and the daytime asymmetry toward higher temperatures is even more pronounced. This may be an expression not only of thermal emissions from soil and forest floor materials, through the incomplete foliar canopy on this site, but also from some large openings of bare soil and rock. Also, the distributions are irregular, with no particular most-frequent class, or mode, of temperature values.

Showing even more contrast in frequency distribution range and pattern is Fig. 1d), for the clearcut site (SNOW). Several differences from the other patterns are apparent: The asymmetry of the daytime distributions are reversed, with limbs

Table 1. TIMS-Observed Surface Temperature Statistics for Sites on the H. J. Andrews Experimental Forest, 5 Aug. 1985[a]

Site ID	Surface Type	Temperature (°C)					Form Factor	Max Freq %
		Low	High	Range	Mean	DISPRS		
				Daytime				
AS32-D1	Forest	25.4	34.3	8.9	28.19	6.99	7.46	8.8
AS32-D2	Forest	26.7	34.6	7.9	29.04	6.41	9.46	10.8
L341-D1	Natural-regen.	21.6	50.0	28.4	28.51	22.79	3.23	5.9
L341-D2	Natural-regen.	22.7	53.1	30.4	30.17	24.45	3.13	5.3
L521-D1	Plantation	19.8	40.8	21.0	29.22	16.70	2.93	6.2
L521-D2	Plantation	26.2	40.8	14.6	29.98	14.34	5.65	7.0
OLDG-D1	Forest	20.6	32.3	11.7	24.19	7.29	3.33	8.6
OLDG-D2	Forest	21.6	34.8	13.2	25.10	6.01	4.59	12.5
ROCK-D1	Quarry	27.9	59.2	31.3	48.47	44.90	− 2.28	3.9
ROCK-D2	Quarry	44.5	60.1	15.6	52.97	15.97	0.22	4.5
RS07-D1	Forest	24.2	42.5	18.3	27.40	9.50	4.16	10.1
RS07-D2	Forest	25.7	37.7	12.0	28.31	6.23	5.52	11.1
RS10-D1	Forest	25.9	34.8	8.9	28.39	7.22	7.88	10.1
RS10-D2	Forest	27.1	33.7	6.6	29.18	5.33	8.32	12.3
RS18-D1	Forest	20.4	31.1	10.7	23.99	8.89	7.72	10.6
RS18-D2	Forest	21.1	30.2	9.1	24.67	6.89	1.91	13.0
SNOW-D1	Clearcut	24.5	60.8	36.3	50.48	37.64	− 2.03	2.7
SNOW-D2	Clearcut	40.6	60.4	19.8	52.64	21.51	− 2.10	2.7
MNDL-D1	Shelterwood	31.8	60.8	29.0	52.52	36.93	− 2.12	2.6
MNDL-D2	Shelterwood	32.3	60.8	28.5	51.96	38.36	− 1.93	2.4
				Nighttime				
AS32-N1	Forest	18.2	22.9	4.7	20.79	5.04	− 0.50	15.7
AS32-N2	Forest	17.7	21.6	3.9	20.14	4.01	− 11.35	18.8
L341-N1	Natural-regen.	13.5	19.8	6.3	16.38	6.43	0.72	10.0
L341-N2	Natural-regen.	12.9	19.6	6.7	15.93	6.74	2.16	12.4
L521-N1	Plantation	10.0	19.8	9.8	16.59	6.78	− 9.01	22.8
L521-N2	Plantation	10.0	19.8	9.8	16.09	6.55	− 9.98	17.3
OLDG-N1	Forest	18.5	21.1	2.6	19.52	2.31	22.79	32.0
OLDG-N2	Forest	18.0	20.4	2.4	19.11	2.78	5.32	24.5
ROCK-N1	Quarry	16.9	22.7	5.8	17.50	6.73	− 6.32	11.3
ROCK-N2	Quarry	20.4	24.5	4.1	21.54	3.39	16.43	30.3
RS07-N1	Forest	20.1	23.4	3.3	22.45	3.01	− 22.76	24.5
RS07-N2	Forest	19.3	23.2	3.9	21.98	3.40	− 21.42	29.7
RS10-N1	Forest	20.4	22.9	2.5	21.66	2.77	− 6.14	24.4
RS10-N2	Forest	20.6	22.4	1.8	21.47	2.28	8.03	26.8
RS18-N1	Forest	18.0	20.1	2.1	19.02	2.25	12.70	26.7
RS18-N2	Forest	15.7	19.8	4.1	18.50	3.09	− 11.58	24.4
SNOW-N1	Clearcut	11.5	21.9	10.4	16.32	9.98	0.62	7.3
SNOW-N2	Clearcut	10.6	20.4	9.8	15.77	9.95	− 0.91	8.7
MNDL-N1	Shelterwood	16.6	21.1	4.5	16.77	3.62	− 4.95	19.5
MNDL-N2	Shelterwood	16.6	22.4	5.8	17.89	5.41	12.25	16.0

[a] D = day, N = night, 1 = first flight, and 2 = second flight.

graduating toward cooler temperatures, instead of warmer; both the daytime and nighttime frequency distributions have even lower frequency percentages, making it more difficult to identify any dominant mode in the frequency distributions; and both day and night frequency distributions extend over wide temperature ranges, spanning the entire thermal image range. The daytime frequency distributions express the effects of this surface's micro relief which produced many facets that were exposed to the sun at diverse angles to take on a wide range of temperatures. The gradual extension from the modal classes to cooler temperatures may be due to the rather sparse coverage by herbaceous vegetations. Most of the vegetation was senescent, and therefore not transpiring. Had it been live, perhaps even lower surface temperature classes would likely have been observed.

The shelterwood site (MNDL), Fig. 1e), is similar to the daytime pattern of the clearcut, having a slowing rising frequency distribution toward higher temperatures. But its nighttime pattern resembles that of a forested site. Shelterwoods are typically logged to leave approximately four to eight large Douglas-fir trees per hectare, presumably mediating the microclimate in favor of forest regeneration. The soil surface of this particular site is more steeply inclined toward south, and closer to the canyon bottom than the others. During D1 and D2, it was exposed to solar radiation at near-normal incidence, as well as to longwave emissions and reflected solar radiation from adjacent slopes in the canyon. Highest temperatures for this site were beyond the scale expressed in the daytime datasets. And daytime temperature frequency distributions were irregular, with adjacent temperature classes having widely ranging frequencies, yielding discontinuous frequency distributions. This is in contrast to the other sites. It is as if the surface is composed of discrete facets, with some temperature classes essentially missing. While the clearcut showed some of this, the expression is more dramatic on the shelterwood, and may have been due to the effects of shading by the remaining large trees.

The dataset from the rock quarry (ROCK), Fig. 1f), completes this graphical summary of the variety in observed frequency distributions. This site is on a minor peak on the northern boundary line of the H. J. Andrews. It exhibits the most irregular pattern of those observed. Part of this is probably due to its smaller area, and thus small number of pixels. But the rock quarry's daytime datasets tend to extend and confirm interpretations of the discontinuous types of pattern seen in the clearcut and shelterwood site datasets. Unfortunately, the nighttime patterns are not consistent with each other, it appearing likely that the N2 frequency distributions were mistakenly taken from the adjacent forested area.

Table 1 lists the measured characteristics and statistical properties of the frequency distributions for all 10 sites. The tabulated values quantify the features seen in Fig. 1. The low, high, and range temperatures are the measured lowest and highest dataset pixel values, and their difference. The mean is the statistical central moment of the measured pixel temperatures. The other three entries in the table are: 1) The width of the frequency distributions, or statistical measure of dispersion, is DISPRS. It is computed as ± 3 times the standard deviation of the frequency distributions. 2) The form factor is the ratio of the frequency distribution's third and fourth moments, normalized by the temperature scale. This statistical property was computed to represent the frequency distribution's peakedness and symmetry. Unfortunately, the form factor is very sensitive to any irregularities in the frequency distributions, so its intended use for pattern interpretation was not achieved. 3) The distribution's height, the measured greatest frequency of occurrence, is max freq %.

MODEL DEVELOPMENT

It is evident that the various surface temperature frequency distribution patterns are characteristic of the type of surface from which they were observed. The patterns are expressive of the thermal properties and microclimates of those surfaces. Some generalizations about the expected behavior of these surface types, based on the observed patterns, are:

1. Daytime, sunlit-surface temperature frequency distribution patterns vary more widely than nighttime frequency distributions, and are quite sensitive to the site's spatial uniformity, i.e., whether or not a surface is composed of many elements or facets of differing temperatures.

2. Daytime frequency distributions tend to be dominated and narrowed by foliage, particularly when the foliage is a coniferous canopy.
3. Single-moded, sharply-peaked frequency distributions characterize nighttime forested surfaces. The nighttime frequency distributions from a non-forested surface is broader.
4. Although limited by the size of individual pixels, the observed surface temperature frequency distribution defines the spatial temperature domain of the site at the time of image acquisition. Depending on the correspondence of pixel size to the size of predominating surface features, there is some suggestion of a potential for partitioning the daytime imaged area according to the various components making up the surface, e.g., vegetated, nonvegetated portions, particularly if model definitions for certain types of surface can be employed as reference standards.
5. Conceptually, nighttime pixel temperatures might be similarly partitioned, although their narrow temperature ranges would make vegetated/nonvegetated discrimination more difficult. The observed nighttime temperature frequency distributions were expressing different dissipative response mechanisms than those during the day, but did seem to behave differently for vegetated surfaces than for bare soil or rock.
6. The aggregate effects, considering both daytime and nighttime temperature behaviors, should aid in understanding the extent to which surface microclimates can be altered by land management practices. And the site-by-site analysis of those microclimates should be extendable toward a more accurate expression of the effects of surface alteration on climatic behaviors at larger scales.

The BETA Probability Distribution as a Model for Describing the Frequency Distributions of Surface Temperature

In statistics the term frequency refers to the number of occurrences an observed value occurs within a specified interval. Frequency distributions are graphically depicted by histograms. The sum total of all possible occurrences drawn from a population has unity, or 100%, probability. This integral function of the individual probabilities over all intervals defines the probability distribution.

On the other hand, the term probability density function, or PDF (Lumley and Panofsky, 1964) refers to the derivative function of a probability distribution, usually after it has been smoothed. If not smoothed or its behavior generalized in some way, the PDF and the frequency distribution would otherwise be equivalent.

The bell-shaped Gaussian, or normal, distribution is the most commonly applied example of a PDF. When a hypothesis of normality is acceptable, the distribution of sampled datasets is usually not of primary concern. And, as a practical matter, frequency distributions constructed from sample datasets are often insufficient for defining the statistical attributes of any other distribution. However, it is apparent that few, if any, of the observed temperature frequency distributions in this study would classify as normal distributions, necessitating the choice of some alternative distribution.

The popularity enjoyed by the normal distribution is attributable to its existing body of well-developed theory, which also defines its statistical behavior, and the likelihood that most sampled datasets can rarely be shown to depart from a normal distribution. This distinction, separating a frequency distribution histogram from a PDF, has no doubt arisen owing to: 1) historical considerations of the continuous versus discrete properties of observations (particularly in small samples drawn from larger populations); 2) the analytical advantage of being able to depict frequency distributions in mathematically deterministic ways; and 3) the limited degree to which observational data typically represents the populations from which the samples were taken.

In consideration of the above discussion, and somewhat in contrast to the restrictions noted, the datasets for the TIMS imaged sites in this study will hereafter be regarded as completely representing the populations of thermal pixels, rather than merely being a small sample drawn from that population. Further, the data interval is small ($\pm 0.2°C$) and continuous, without inadvertent sampling gaps, rather than discrete, randomly sampled packets of information. Therefore, the term PDF could be applied to the frequency distributions of the observed TIMS datasets.

The regularity of the frequency distribution patterns of the TIMS datasets, and their disimilar-

ity to a normal distribution, prompted our selection of the beta probability distribution for the modeling effort. The beta distribution (Selby, 1968; Press et al., 1986) can take on a large range of shapes, thereby having the potential to categorically describe many observed distributions. The statistical properties of beta probability distributions are well known, and a beta probability distribution can be fitted to any closed distribution assumed to have a single mode. It is defined by two parameters and a gamma function (Γ) (op. cit.) of these same parameters:

$$f(x) = \Gamma(\alpha, \beta)\left[(x)^{\alpha} * (1-x)^{\beta}\right],$$

$$\text{for} \quad 0 < x < 1 \quad \text{and} \quad \alpha > -1, \beta > -1. \quad (1)$$

Note that the distribution is a closed one, owing to the term in square brackets, which forces a return to zero at each end of the x range. The position along the x scale is governed by the relative sizes of α to β: When $\alpha > \beta$, the distribution is shifted to the right, and vice versa; if $\alpha = \beta$, the mean of the distribution is 0.5, and may be made to look very much like a normal distribution. The range of the distribution narrows as α and β are made larger. For integer values of α and β, the gamma function term is

$$\Gamma(\alpha, \beta) = \frac{[\Gamma(\alpha+\beta+2)]}{[\Gamma(\alpha+1)\Gamma(\beta+1)]} \qquad (2)$$

defining $\Gamma(y) = (y-1)!$, where ! is the factorial operator and y is the sum of values in parentheses.

The role of the gamma function is an important and primary one. It can be interpreted as a weighting coefficient, or third parameter, which conditionally assures that the integral of the BETA $f(x)$ distribution is equal to 1 (unity probability) for any α, β values that may be chosen. Because of this condition, $f(x)$ can truly be regarded as an estimator of the probability of x, i.e., $p(x)$, for datasets being fitted by a BETA distribution.

Fitting BETA Probability Distributions to Observed Frequency Distributions

Modeling a Frequency Distribution of Surface Temperature with a BETA Probability Distribution.

Each TIMS dataset was modeled with a BETA probability distribution. The following describes the steps used:

1. Scale the TIMS temperature values, from the observed frequency distribution dataset, to range from 0 to 1:

$$x = \frac{T_j - T_{\text{low}}}{T_{\text{high}} - T_{\text{low}}}$$

low and high being the extreme TIMS values, and

$$T_{\text{low}} \le T_j \le T_{\text{high}}.$$

2. Choose values for α, β, and compute for each x:

$$(x)^{\alpha} * (1-x)^{\beta}.$$

Near 0 and 1 of x, this BETA product function can produce very small numeric values. Computational difficulties may also arise when the frequency distribution is narrow and has large frequency classes, situations that necessitate choosing large values of α or β.

3. Find the integral function from step 2 for all x:

$$0 \le x \le 1.$$

This is done by successively summing the results of step 2 for x over its 0–1 range.

4. Normalize the function described by step 3 according to its value at $x = 1$. In step 3, this maximum value will likely be a small number. Dividing it into all values of the function produced in step 3 will result in a function being produced by this step (step 4), which is a cumulative BETA distribution with an integral value of unity at $x = 1$. This step performs an equivalent operation to the coefficient $\Gamma(\alpha, \beta)$, which is troublesome to compute.
5. Differentiate the resultant function of step 4 at the intervals of x. This produces the BETA probability density function (PDF) of α, β, or $p(x)$.
6. Compare $p(x)$ with the observed frequency distribution. Loop iteratively through step 2 (selecting new trial values of α, β) to step 6 until an acceptable level of comparability is found. For the cases shown here, a combination of least squares fit and visual (graphical) matching at the modal frequency was used. This combination approach helped avoid

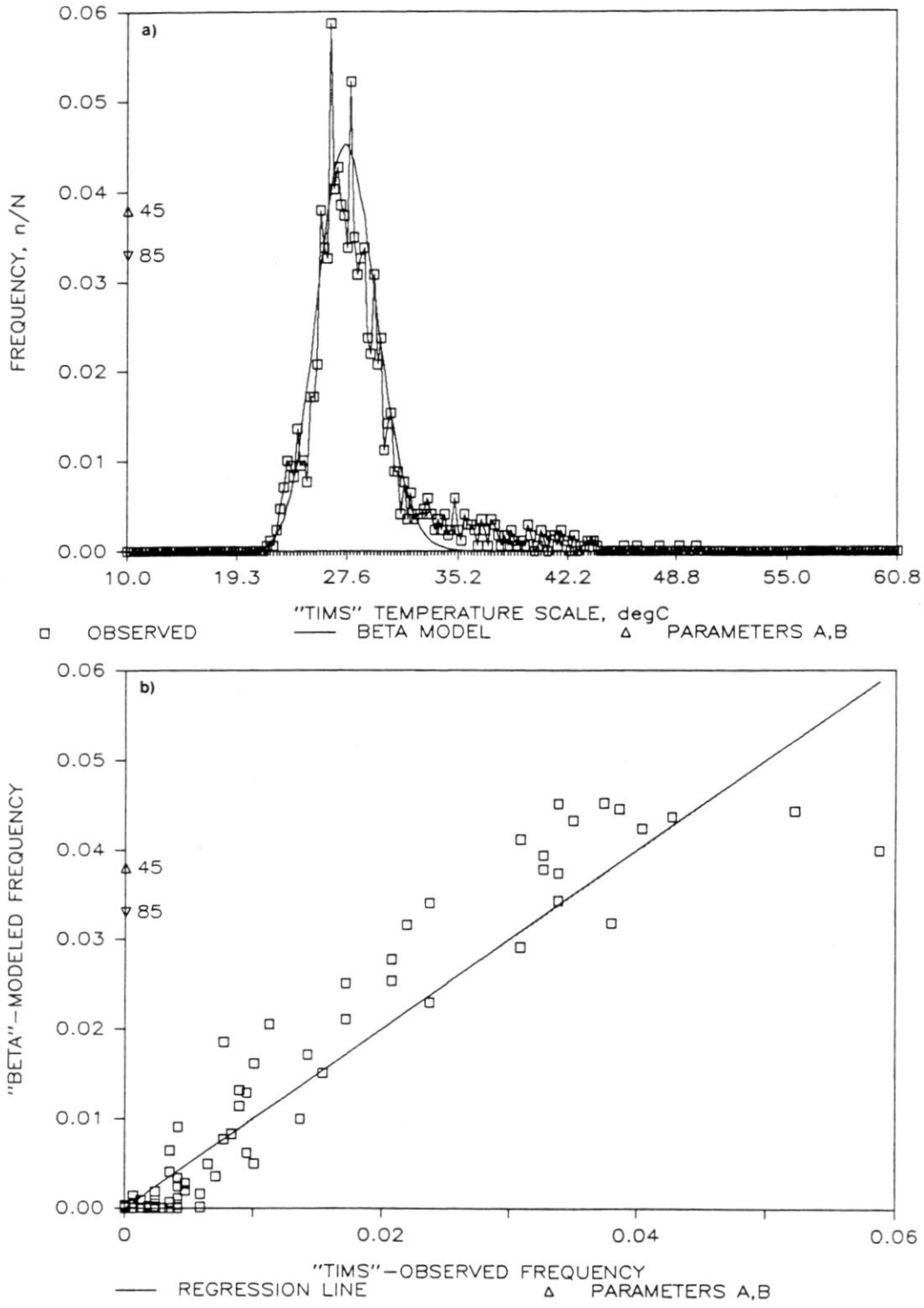

Figure 2. An example of a BETA modeled surface temperature frequency distribution. a) TIMS frequency observations (-□-), superimposed with BETA model frequency estimates (—). The BETA parameters A and B (△) producing this "fit" are shown along the Y-axis, α above β. b) An $X-Y$ scatterplot and the "fitted" regression line for the frequency distributions shown in 2a). Procedures are detailed in the text.

choosing the α, β parameter set which may yield a high regression coefficient, but which did not simultaneously represent the modal class of the observed distribution.

An Example of a BETA-Modeled Surface Temperature Distribution

Figure 2a) shows an example, for the H. J. Andrews site: "natural regeneration" (L341), of both the observed frequency distribution of surface temperature data and the results of a BETA distribution fit, developed using the procedure described above. This particular example is from daytime TIMS overflight number 1 (D1). The values of the parameters α, β which were used to produce the BETA results (the smooth curve superimposed through the connected data points in Fig. 2a) are shown to the right of the Y-axis (45, 85). The major feature of the frequency distribution of surface temperature can be seen to be fairly closely described by the BETA probability distribution.

Unlike Fig. 1c), for the same site, which shows data from all four overflights, Fig. 2a) allows more of the detail to be seen. Upon inspection, 2 peaks (or modes) in the dataset are evident, as is the pronounced limb in the frequency distribution, extending toward high surface temperatures. While the BETA distribution does not describe all of these details, it does follow the general character of the observed frequency distribution. One measure of how well the model fits is obtained by regression. For this example (L341-D1), R^2 is 0.923.

The regression test was made a part of the fitting procedure. The fitting procedure utilized only those frequencies within the TIMS-observed pixel temperature range, excluding of the tails of the BETA distribution, which were beyond the low–high range of the dataset. Using the regression, various values of α, β were tried, iteratively, until a maximum R^2 was found. Tabulating the resulting R^2 values in the form of a matrix with coordinates α, x, β helped in the process of choosing the best parameter combination. Using such a matrix table, the optimal α, β values were chosen from along what appears as a diagonal "ridge" of higher correlation coefficients. This iterative technique was also assisted by viewing graphs of the "fit" on a graphics monitor, since the convergence of α, β values toward an optimum could be visually evaluated, especially during the early stages of fitting. Additionally, viewing the fit helped assure against selecting α, β values that may happen to yield a high R^2, but failed to satisfactorily produce the frequency near the principle mode of the distribution. This was often the situation for the more irregular datasets. As a figure of merit, R^2 may not be the optimal choice, and its maximum was sometimes quite broad through a range of α, β values, but it is an easy one to implement. Also, in view of the wide range in α, β combinations, representing all observed surface temperature distributions in the Andrews' datasets, the regression-fitting technique seemed to provide fairly adequate discrimination among the sites examined.

Figure 2b) is the $X-Y$ scatterplot of TIMS versus BETA regression for the "natural regeneration" (L341-D1) site. The two peaks (modes) in the frequency distribution are expressed to the right and below the regression line; and the observations along the right limb of the frequency distribution, which had frequencies below 0.05, are grouped near the origin. Otherwise, the clustered pattern of data points around the regression line, which has slope 1.026, was judged an acceptable fit.

Results of BETA Distribution Fits for 10 Sites on the Andrews Experimental Forest

The fitting procedure was repeated for all 40 datasets; 10 sites by four imaging overflights. The results are presented in Table 2. In addition to the α and β BETA parameters, a BETA index (derived from the parameters and defined in the next section), and the R^2 (R-SQRD) values, the table presents model-estimated values for mean surface temperature, temperature dispersion (DISPRS), mode temperature, and modal frequency (mode freq %). Unlike the observed distributions, these latter two properties can be precisely defined, owing to the deterministic nature of the model. Ideally, the mean should be the same as the value calculated from the data, and might have been chosen as a fitting criterion. But the irregularity in some of the observed distributions detracted from its suitability for this purpose. The model dispersion value (DISPRS) was calculated the same way (± 3 standard deviations) as it was for the datasets. Again, because the model has no randomness, and its statistical properties are determined by the parameters of the model, model DISPRS will be

more conservative (smaller) than the comparable statistic based on observational values.

The BETA Index and Site Rankings

To make ranked comparisons between the sites, the two BETA parameters were combined into a single value, the BETA index. This index contains information about both the parameter ratio and parameter magnitudes. The fitted α, β values for the sites had absolute ratios of less than 1 to above 3, at the same time ranging over 3 orders of magnitude; $1 < \alpha$ or $\beta < 1000$, or more. The geometric mean (GM) of $\alpha, \beta, \sqrt{\alpha * \beta}$ was selected to represent magnitude information. The logarithm of the β/α ratio (LR), $\log(\beta/\alpha)$, was chosen to convey the relationship between α and β. The advantage of this logarithmic form was twofold: first, it indicates model asymmetry in a manner similar to the third moment of the dataset; and second, it

Table 2. BETA-Modeled Surface Temperature Distributions for Sites on the H. J. Andrews Experimental Forest, 5 Aug. 1985[a]

		BETA Parameters			*Fit*	*Temperature (°C)*			*Mode*
Site ID	*Surface Type*	*A*	*B*	*Index*	R^2	*Mean*	*DISPRS*	*Mode*	*Freq %*
				Daytime					
AS32-D1	Forest	178	320	60.8	0.953	28.18	6.57	28.1	8.8
AS32-D2	Forest	250	420	73.0	0.963	28.98	5.68	28.8	9.8
L341-D1	Natural-regen.	45	85	17.1	0.923	27.64	12.69	27.4	4.5
L341-D2	Natural-regen.	55	95	17.2	0.925	28.68	11.95	28.6	4.7
L521-D1	Plantation	70	120	21.5	0.942	28.76	10.63	28.6	5.3
L521-D2	Plantation	120	200	34.4	0.925	29.08	8.22	29.1	6.8
OLDG-D1	Forest	95	245	62.8	0.989	24.22	7.40	24.2	8.1
OLDG-D2	Forest	240	570	138.9	0.984	25.06	4.86	24.9	12.0
ROCK-D1	Quarry	23.5	5	−7.3	0.423	52.01	21.14	53.1	2.1
ROCK-D2	Quarry	41	8	−12.9	0.620	52.58	15.86	53.3	2.8
RS07-D1	Forest	215	420	87.4	0.986	27.21	5.73	27.1	10.1
RS07-D2	Forest	265	470	87.8	0.987	28.33	5.42	28.4	10.5
RS10-D1	Forest	195	350	66.4	0.954	28.20	6.29	28.1	9.2
RS10-D2	Forest	310	515	88.1	0.983	29.11	5.12	29.1	10.9
RS18-D1	Forest	130	350	91.7	0.952	23.78	6.17	23.7	9.8
RS18-D2	Forest	210	520	130.1	0.927	24.63	5.09	24.5	11.6
SNOW-D1	Clearcut	23	5	−7.1	0.900	51.86	21.46	53.0	2.1
SNOW-D2	Clearcut	20	4	−6.3	0.896	52.48	22.45	53.9	2.0
MNDL-D1	Shelterwood	7.7	1.3	−2.4	0.562	53.76	32.78	58.7	1.7
MNDL-D2	Shelterwood	7.5	1.4	−2.4	0.477	53.14	34.14	57.8	1.5
				Nighttime					
AS32-N1	Forest	160	600	177.9	0.837	20.69	4.38	20.6	13.5
AS32-N2	Forest	150	600	180.6	0.913	20.18	4.40	20.1	13.8
L341-N1	Natural-regen.	25	170	54.3	0.969	16.54	7.30	16.3	9.2
L341-N2	Natural-regen.	32	245	78.3	0.843	15.88	5.87	15.7	11.5
L521-N1	Plantation	135	850	270.7	0.899	16.96	3.29	16.9	19.5
L521-N2	Plantation	100	700	223.6	0.963	16.36	3.56	16.3	18.7
OLDG-N1	Forest	272	1170	357.4	0.735	19.59	3.15	19.6	20.2
OLDG-N2	Forest	260	1200	371.0	0.918	19.05	3.05	19.0	20.9
ROCK-N1	Quarry	75	320	97.6	0.597	19.67	5.99	19.6	10.4
ROCK-N2	Quarry	295	1000	288.0	0.807	21.56	3.66	21.6	17.8
RS07-N1	Forest	300	900	247.9	0.847	22.52	2.90	22.7	19.5
RS07-N2	Forest	300	990	282.6	0.605	21.80	3.62	21.9	17.7
RS10-N1	Forest	300	1000	286.4	0.946	21.71	3.62	21.6	17.8
RS10-N2	Forest	300	1000	286.4	0.603	21.67	3.33	21.6	18.5
RS18-N1	Forest	250	1150	355.4	0.944	19.07	3.06	19.0	20.5
RS18-N2	Forest	230	1150	359.5	0.938	18.48	2.97	18.5	21.0
SNOW-N1	Clearcut	14	95	30.3	0.930	16.57	9.79	16.1	6.9
SNOW-N2	Clearcut	13	95	30.4	0.830	16.15	9.57	15.7	7.1
MNDL-N1	Sheterwood	192	850	261.0	0.971	19.37	3.70	19.3	17.3
MNDL-N2	Shelterwood	168	775	239.6	0.967	19.06	3.81	19.0	16.8

[a] D = day, N = night, 1 = first flight, 2 = second flight.

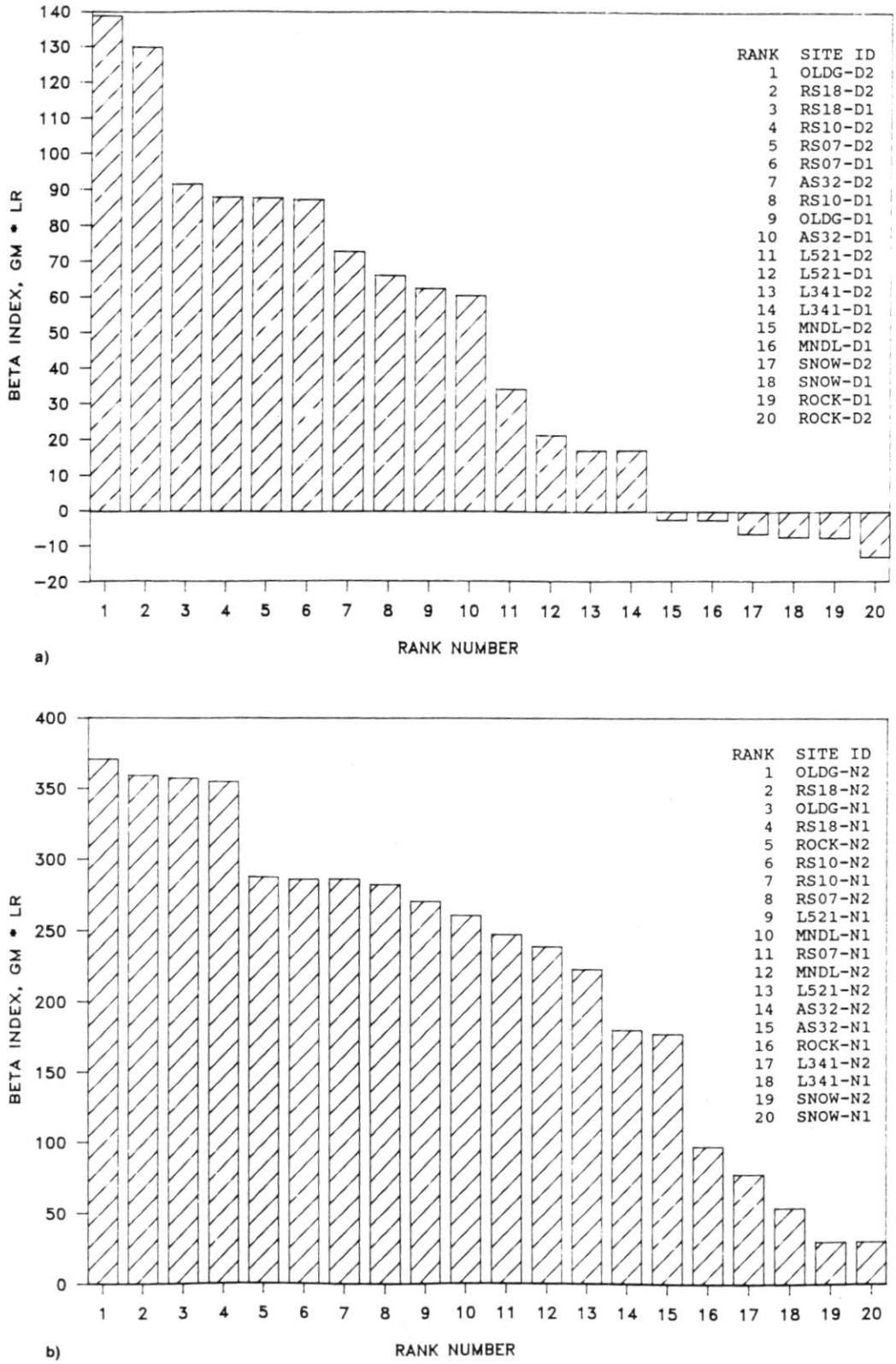

Figure 3. Site rankings, according to the parameter-based BETA index: GM * LR (see text). a) Daytime results; b) nighttime results. See legend for site identifications.

offers greater discrimination between distributions having ratios close to unity, essentially stretching the contrast level for scenes with narrow and/or nearly symmetrical temperature frequency distributions, i.e., the nighttime datasets. The BETA index was formed as the product of these two terms: GM * LR.

Figure 3 shows a ranking of the sites according to their BETA index values. Figure 3a) shows the results for the daytime datasets; Fig. 3b), for nighttime. The daytime rankings are consistent with intuition, as all the forested sites group toward one end (large positive BETA indices), graduating down toward the lower canopy densities and the barren sites, which also show negative BETA index values, consistent with their negatively skewed frequency distributions (negative third moments). This trend supports our interest in using the BETA model as a tool for distinguishing sites on the basis of cover type. As would be expected, site discriminating power corresponds to the amount of temperature contrast in the scene. Thus, the nighttime ranking does not yield as clear a separation among sites as the daytime. The nighttime ranking embarrassingly revealed that our second dataset for the ROCK site was, in fact, drawn from the forest adjacent to it (rank position 5).

CONCLUSIONS

BETA probability distribution models of TIMS spatial surface temperature frequency distribution data have described landscapes at the H. J. Andrews Experimental Forest quite well. By providing simply parameterized descriptions of those distributions, this image analysis technique appears to have considerable advantages over the use of ensembled statistical descriptions. Acquisition of additional TIMS datasets from widely different landscape types are needed to test the BETA model's general applicability.

Some of the applications we anticipate for BETA-modeled surface temperature frequency distributions have already been discussed in previous sections. In summary, they include: classifying landscapes on the basis of their thermal images; interrelating such classifications with ecological processes; evaluating alternative land management strategies in microclimatic terms, as interpretable from the thermal image data; and, developing composite-surface heat balance models for predicting regional climate impacts.

This work was funded by NASA's Terrestrial Ecosystems Program (RTOP #677-21-29-03). The authors wish to thank the following Lockheed-LESC employees for their valuable contributions: Bill Colliver, Duane O'Neal, Julius Baham, and Sharon Hatch.

REFERENCES

Anderson, J. E. (1985), Thermal infrared data: its characteristics and use, *Am. Soc. Photogramm. Remote Sens. Technol. Pap.* 1:143–155.

Balick, L. K., and Wilson, S. K. (1980), Appearance of irregular tree canopies in nighttime high-resolution thermal infrared imagery, *Remote Sens. Environ.* 10:299–305.

Bartholic, J. F., Namken, L. N., and Wiegand, C. L. (1972), Aerial thermal scanner to determine temperatures of soils and of crop canopies differing in water stress, *Agron. J.* 64:603–608.

Carson, D. J. (1982), Current parameterization of land-surface processes in atmospheric general circulation models, in *Land Surface Processes in Atmospheric General Circulation Models* (P. S. Eagleson, Ed.), pp. 67–108.

Carlson, T. N. (1986), Regional-scale estimates of surface moisture availability and thermal inertia using remote thermal measurements, *Remote Sens. Rev.* 1:197–247.

Childs, S. W., Holbo, H. R., and Miller, E. L. (1985), Shadecard and shelterwood modification of the soil temperature environment, *Soil Sci. Soc. Am. J.* 49:1018–1023.

Dickinson, R. E. (1983), Land surface processes and climate-surface albedos and the energy balance, *Adv. Geophys.* 25:305–353.

Fritschen, L. J., Balick, L. K., and Smith, J. A. (1982), Interpretation of infrared nighttime imagery of a forested canopy, *J. Appl. Meteorol.* 21:730–734.

Gates, D. M. (1962), *Energy Exchange in the Biosphere*, Harper and Row, New York, 151 pp.

Graham, M. H., Junkin, B. G., Kalcic, M. T., Pearson, R. W., and Seyfarth, B. R. (1986), ELAS-Earch Resources Laboratory Applications Software, revised Jan. 1986, NASA/NSTL/ERL Report No. 183.

Hatfield, J. L., Reginato, R. J., Jackson, R. D., Idso, S. B., and Pinter, P. J., Jr. (1983), Evapotranspiration Estimates from Surface Temperature Input to a Surface Energy Balance Model, Proc. 16th Conf. Agric. and Forest Meteorol., pp. 79–80.

Hatfield, J. L., Reginato, R. J., and Idso, S. B. (1984), Evaluation of canopy temperature–evapotranspiration models over various surfaces, *Agric. Forest Meteorol.* 32:41–53.

Hawk, G. M., Franklin, J. F., McKee, W. A., and Brown, R. B. (1978), H. J. Andrews Experimental Forest Reference stand system: establishment and use history, IBP Conif. Forest Biome Bull. 12, 79 pp.

Heilman, J. L., Kanemasu, E. T., Rosenberg, N. J., and Blad, B. L. (1976), Thermal scanner measurement of canopy temperatures to estimate evapotranspiration, *Remote Sens. Environ.* 5:137–145.

Holbo, H. R., and Childs, S. W. (1987), Summertime radiation balances of clearcut and shelterwood slopes in southwest Oregon, *Forest Sci.* 33:504–516.

Holbo, H. R., Childs, S. W., and McNabb, D. H. (1985), Solar radiation at seedling sites below partial canopies, *Forest Ecol. Manage.* 10:115–124.

Idso, S. B., Jackson, R. D., and Reginato, R. J. (1975), The utility of surface temperature measurements for the remote sensing of surface soil water status, *J. Geophys. Res.* 80:3044–3049.

Idso, S. B., Jackson, R. D., and Reginato, R. J. (1977), Remote sensing of crop yields, *Science* 189:1012–1013.

Kneizys, F. X., Settle, E. P., Gallery, W. O., Chetwynd, J. H., Jr., Abreu, L. W., Selby, J. E. A., Fenn, R. W., and McClatchey, R. A. (1983), Atmospheric transmittance/radiance: computer code Lowtran-6, Air Force Geophysics Laboratory Rep. AFGL-TR83-0187, Optical Physics Division, Hanscom Air Force Base, MA 01731, 200 pp.

Lumley, J. L., and Panofsky, H. A. (1964), *The Structure of Atmospheric Turbulence*, Wiley-Interscience, New York, 239 pp.

Palluconi, F. D., and Meeks, G. R. (1985), Thermal Infrared Multispectral Scanner (TIMS): an investigator's guide to TIMS data, JPL Pub. 85-32, 14 pp.

Press, W. H., Flannery, B. P., Teulosky, S. A., and Vetterling, W. T. (1986), *Numerical Recipes*, Cambridge Univ. Press, Cambridge, 818 pp.

Price, J. C. (1980), The potential of remotely sensed thermal infrared data to infer surface soil moisture and evaporation, *Water Resources Res.* 16:787–795.

Price, J. C. (1982), Estimation of regional scale evapotranspiration through analysis of satellite thermal-infrared data, *IEEE Trans. Geosci. Remote Sens.* GE-20:286–292.

Reginato, R. J., Jackson, R. D., and Pinter, P. J., Jr. (1985), Evapotranspiration calculated from remote multispectral and ground station meteorological data, *Remote Sens. Environ.* 18:75–89.

Sader, S. A. (1986), Analysis of effective radiant temperatures in a Pacific Northwest forest using thermal infrared multispectral scanner data, *Remote Sens. Environ.* 19:105–115.

Sequin, B. (1984), Estimation de l'evapotranspiration a part ir de l'infra-rouge thermique, Proc. 2nd Int. Coll. Spectral Signatures of Objects in Remote Sensing, Bordeaux, France, pp. 427–446.

Seguin, B., and Itier, B. (1983), Using midday surface temperature to estimate daily evaporation from satellite thermal IR data, *Int. J. Remote Sens.* 4(2):371–383.

Selby, S. M., Ed. (1968), *Standard Mathematical Tables*, 16th ed., Chemical Rubber Co., Cleveland, OH, 692 pp.

Shukla, J., and Mintz, Y. (1982), Influence of land-surface evapotranspiration on the earth's climate, *Science* 215: 1498–1501.

Soer, G. J. R. (1980), Estimation of regional evapotranspiration and soil moisture conditions using remotely sensed crop surface temperatures, *Remote Sens. Environ.* 9:27–45.

Stone, L. R., and Horton, M. L. (1974), Estimating evapotranspiration using canopy temperatures: field evaluation, *Agron. J.* 66:450–454.

Vanderwaal, J. A., and Holbo, H. R. (1984), Needle-air temperature differences of Douglas-fir seedlings and relation to microclimate, *Forest Sci.* 30:635–644.